Nanostructured W–Cr Janus Heterojunctions Prepared by Glancing Angle Deposition for Gas Sensing

Guillem Vilar Soler[1], Hamidreza Gerami[2], Anna Krystianiak[3], Olivier Heintz[3], Nicolas Geoffroy[3], Aurélien Besnard[2], Juan Jimenez[4], Roland Salut[1], María Del Carmen Marco De Lucas[3], Antonio Jesus Santos[4], Francisco M. Morales[4], Nicolas Martin[2], Valérie Potin[3], Jean-Baptiste Sanchez[1,*]

[1] Université Marie et Louis Pasteur, CNRS, Institut FEMTO-ST, F-25000 Besançon, France

[2] Université Marie et Louis Pasteur, SUPMICROTECH, CNRS, Institut FEMTO-ST, F-25000 Besançon, France

[3] Université Bourgogne Europe, CNRS, Laboratoire Interdisciplinaire Carnot de Bourgogne ICB UMR 6303, F-21000 Dijon, France

[4] IMEYMAT: Institute of Research on Electron Microscopy and Materials of the University of Cádiz, E-11510, Puerto Real, Spain

ABSTRACT: In this paper, a nanostructured W-Cr Janus thin film was synthesized using the GLancing Angle Deposition co-sputtering technique. The film was elaborated using pure W and Cr targets positioned at equal and fixed deposition angles of 80°, resulting in vertically aligned bicomponent nanocolumns. The morphological and crystallographic properties of W-Cr Janus thin film were studied before and after an annealing treatment in air, as high as 500°C. Investigations revealed that annealing induces the formation of a fully oxidized surface envelope composed of p-type Cr_2O_3 and n-type WO_3, which non-uniformly covers the Janus nanocolumns. The chemical gas sensor based on the annealed W-Cr Janus thin film demonstrated promising sensing performances, achieving detection limits of approximately 37 ± 5, 26 ± 5, and 36 ± 5 ppb for benzene, formaldehyde, and propanol, respectively. Beyond representing a technical advancement in the field of co-sputtered thin films, this study underscores the potential of this bicomponent heterojunction structure for the detection of trace-level air pollutants.

1. INTRODUCTION

Metal oxide semiconductor (MOS) gas sensors have gained considerable attention in recent decades since they are essential for environmental monitoring, industrial safety, and medical diagnostics.[1] Besides their simplicity and low manufacturing cost, MOS gas sensors provide a wide range of materials, as their semiconducting properties vary according to the atmosphere. The growing need for highly sensitive, selective, and stable gas sensors has driven extensive research into innovative nanomaterials with customized physicochemical properties. Although selectivity remains a challenge, the extensive literature on advanced materials for MOS gas sensor applications showcases a growing trend toward innovative approaches in developing highly sensitive and stable materials. Although tin oxide (SnO_2) remains the reference material, with numerous studies leveraging its remarkable properties for gas sensing,[2] recent years have seen increased interest in other metal oxides that show real potential for the development of more and more efficient sensors.[3, 4] It is well known that the

morphology and dimensions of metal oxides strongly influence the sensing performance of MOS gas sensors.[5, 6] For example, 0D, 1D, 2D or 3D nanostructured materials have been synthesized and studied to evaluate their capacities as sensing layers.[7, 8] These innovative materials are designed, for example, to improve the surface area of the material in order to enhance sensitivity or to lower the operating temperature of sensors.[9-12]

In addition to the material's morphology and dimension, other strategies can enhance detection performances, such as doping with metals (noble or not)[13, 14] or forming heterojunctions.[15, 16] In recent decades, research on heterojunctions has surged, with a strong emphasis on innovative fabrication technologies. The goal is to combine two or more MOS materials in order to achieve better sensing performances than using a single metal oxide. This is mainly because the interface of two individual MOS materials exhibits conspicuous resistance modulation effects, which will further affect the gas sensing performance.[17] These heterojunctions can be categorized into n-n, p-p, or p-n junctions,

depending on the type of materials used. Various elaboration methods can be employed to develop these materials, including the hydrothermal process,[18,19] the sol-gel method,[20,21] thermal evaporation techniques,[22] or pulsed laser deposition.[23] It is worth noting that these materials have been used as sensitive layers for gas sensing applications.

Since the late 1990s, following the work of Brett *et al.* on structured thin films,[24] the GLancing Angle Deposition (GLAD) method has been used in reactive sputtering to grow nanoscale columnar films with controlled and innovative architectures.

(a)

(b)
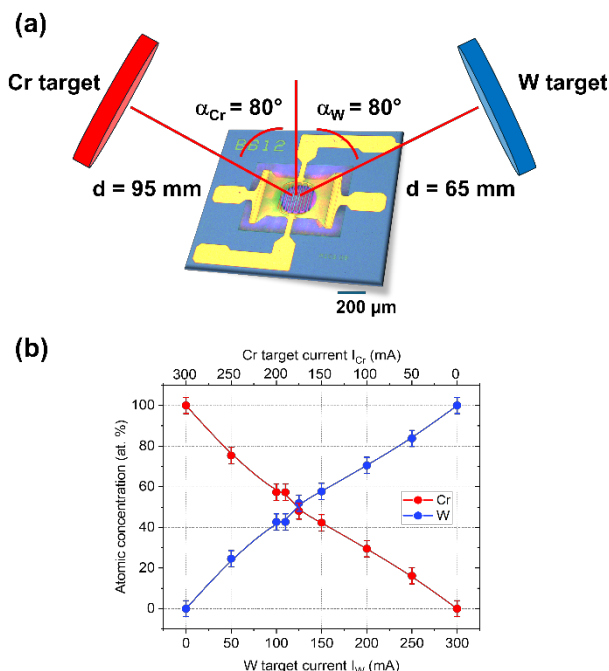
Figure 1: (a) Schematic illustration of the GLAD co-sputtering system implemented to deposit W-Cr Janus thin film onto micro-hotplate (the purple spot indicates the region of the thin film deposition), (b) Evolution of the thin film atomic concentrations of W and Cr with respect to the reverse evolution of target currents.

In most cases, the GLAD process relies on a single source to deposit 3D nanostructured materials such as nanopillars, zigzags, nanospirals, nanotubes or branched nanocolumns.[25-27] The recent development of dual-source deposition is emerging as a promising strategy for producing complex heterojunction thin films with tailored architectures,[28,29] such as Janus structures, in reference to the two-faced Roman God of the same name.[30-33] These thin films structures have asymmetrically designed materials featuring two distinct compositions or functionalities within a single entity. The unique bifunctional nature of Janus structures makes them promising candidates for charge transport and surface reactivity. This is particularly important for the development of chemical gas sensors, as this configuration can improve gas adsorption, thereby enhancing sensing performances in terms of both sensitivity and response time. Despite the versatility of Janus structures fabricated via the GLAD process, to our knowledge, no studies have reported their use for chemical gas sensing application to date. Additionally, it is important to note that the impact of

temperature on this type of nanostructured material has been rarely explored.

However, the literature contains a few studies that have investigated Janus-like nanostructures synthesized using alternative methods for gas sensing applications. For instance, Hu *et al.* reported the fabrication of $ZnO-SnO_2$ Janus nanofibers using electrospinning method for the detection of triethylamine.[34] Wang *et al.* demonstrated the performance of carbon/silica thin film coated on quartz crystal microbalance resonator for the detection of H_2S and NH_3 .[35] Another work on the elaboration of Janus material made of ultrathin gold nanowires and PEDOT:PSS conjugated conducting polymers has been reported by Jiang *et al.* for the identification of ammonia.[36] It is important to note that other studies have been primarily focused on computational approaches to assess the potential of material combinations for the design and development of Janus structures in gas sensing applications.[37-39]

In this paper, we focus on nanostructured W-Cr thin films co-deposited by magnetron sputtering using two different targets: Tungsten and chromium, in order to achieve a Janus nanostructure for gas sensing applications. These two elements were chosen for several reasons: Both exhibit columnar growth,[40,41] share a similar body centered cubic (bcc) structure, and have lattice constants in the same order of magnitude ($a_0(Cr) = 0.288$ nm and $a_0(W) = 0.316$ nm).[42] Furthermore, oxidized tungsten displays n-type behavior, while oxidized chromium exhibits p-type behavior,[43] making their combination promising for the development of heterojunctions. Here, to evaluate the sensing performance of this Janus structure, we selected one volatile organic compound (VOC) -benzene - and two very volatile organic compounds (VVOCs) -formaldehyde and propanol.[44] All these compounds are associated with human activities and considered as indoor air pollutants, even at very low level. Several safety and occupational health authorities worldwide have established permissible exposure limits for inhalation of these compounds. For example, the long-term objective (annual average) limit for benzene is approximately 1.5 ppb (or 1 ppm over an 8-hour period), the 30-minute exposure limit for formaldehyde is around 80 ppb, and the daily exposure limit for propanol is about 280 ppm.[45-47] Prolonged inhalation of these compounds leads to toxic effect for humans.

Beyond the technological challenge of developing highly uniform and homogeneous nanostructured bi-component materials, this paper provides a detailed physico-chemical characterization of W-Cr Janus structures and reports on their potential for air pollutant detection. This work differs from previous studies that primarily investigate the doping of a bulk material (*e.g.*, WO_3 nanoflakes or nanorods) with a small amount of a secondary component (*e.g.*, Cr or Cr_2O_3 nanoparticles),[48,49] whereas in the present study both materials are introduced in nearly equal amounts to form Janus nanocolumns. Since chemiresistive gas sensors typically operate at high temperatures, we also studied the evolution of the nanostructured thin film before and after thermal treatment at temperatures as high as 500 °C. It is important to highlight that only a limited number of studies investigate how Janus materials developed by physical methods evolve with temperature.
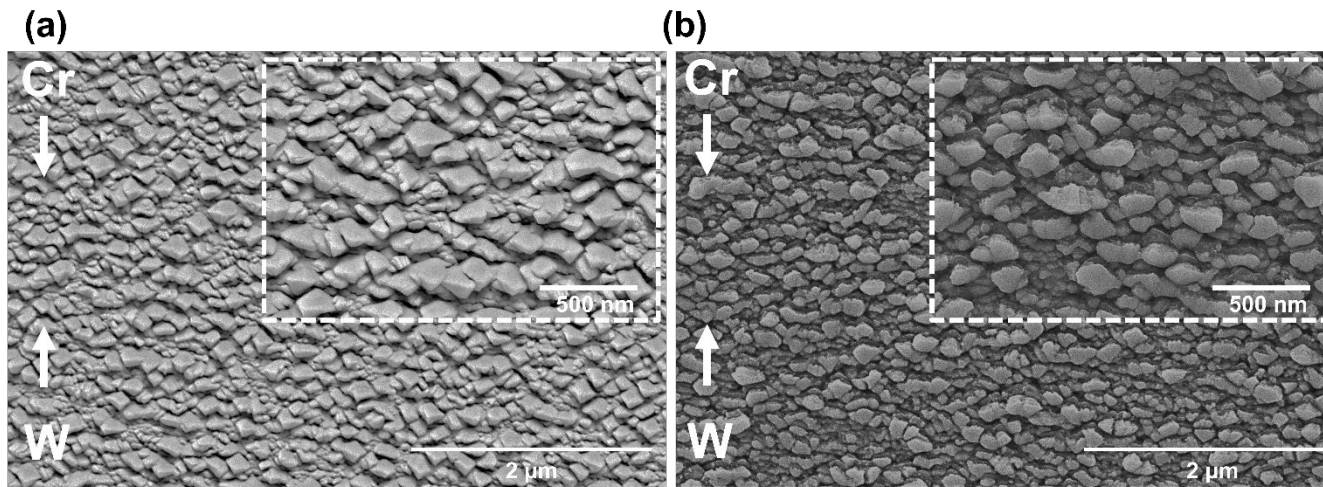
Figure 2: SEM top-view images of the W-Cr Janus thin film: (a) As-deposited and (b) after annealing in air at 250°C for 18 hours, followed by a thermal treatment at 500°C for an additional 6 hours in air. Insets display higher-magnification views. White arrows indicate the flux directions of Cr and W particles during the deposition process.

2. EXPERIMENTAL SECTION

2.1 W-Cr Janus thin film growth

DC magnetron sputtering was used to deposit W-Cr Janus thin films in a homemade vacuum chamber at a base pressure below 10^{-6} Pa. The distance between the substrates and the centers of W and Cr targets were 65 mm and 95 mm, respectively. These targets, having 99.9 at. % of purity and 51 mm diameter, were co-sputtered at room temperature in a pure argon atmosphere with a flow rate of 2.6 sccm and a sputtering pressure of 0.27 Pa. Deposition angles (α_W and α_{Cr}) were both equal and fixed at 80°. W-Cr Janus thin films were produced by carefully and reversely adjusting the current of each target from 0 to 300 mA to achieve a composition with approximately 50 at. % of each material. The deposition time was adjusted to 32 minutes in order to obtain a film thickness of approximately 300 nm. W-Cr Janus films were deposited onto (100) silicon substrates for physico-chemical characterization and also onto commercial micro-hotplate platforms with integrated micro-electrodes for sensing experiments.

2.2 Characterization of material

Elemental compositions were obtained using an XFlash 6 | 60 SDD energy-dispersive X-ray spectroscopy (EDS) detector. The surface views of W-Cr Janus thin films were observed with a Thermo Fisher Scientific Apreo S LoVac scanning electron microscope (SEM). The microstructural analysis was also performed using a TALOS F200X (Thermo Scientific) transmission electron microscope (TEM) operating at 200 kV. Before TEM observations, sample preparation was carried out using focused ion beam (FIB) technique (Thermofisher Helios 5 UC). TEM images were analyzed using GATAN Digital Micrograph software and their simulations were obtained with the Java Electron Microscopy Software (JEMS). The elemental chemical composition was also determined under scanning-transmission (STEM) mode using Super-X EDS system equipped with four windowless SDD detectors. Crystal structure of films was characterized by grazing incidence X-ray diffraction (GIXRD) using a Bruker D8 focus diffractometer with a copper X-ray tube (Cu $\lambda K_{\alpha1}$ = 0.15419 nm). Scans were performed with a step of 0.02° per 8s and a 2θ angle ranging from 20 to 90°. Raman spectra were obtained with a Renishaw inVia spectrometer using a 532 nm laser. X-ray photoelectron spectroscopy (XPS) data were obtained with a PHI VersaProbe I system using a non-monochromatized Al Kα X-ray source (hν = 1486.7 eV, power of 50 W). Energy calibrations were done on adventitious carbon (CC/CH bonds) at 248.8 eV. CasaXPS software was used for data treatment.

2.3 Fabrication of gas sensors and measurements

For sensing tests, W-Cr thin films were deposited onto micro-hotplate platforms from SGX Sensortech, equipped with interdigitated electrodes and allowed both the heating control and conductance measurement of the sensitive material as a function of time (cf. Fig. 1 (a)). In this case, a specially designed shadow mask was employed to selectively deposit materials onto interdigitated micro-electrodes, resulting in a sensitive area of approximately 0.0314 mm² (see the purple spot in Fig. 1 (a) reflecting the W-Cr thin film). Before exposing the sensor to pollutants, a conditioning sequence was performed to progressively age the sensitive surface. This process involved exposing the sensor to a synthetic air flow (mixture of nitrogen 80 vol. % and oxygen 20 vol. % with low levels of water (∼ 2 % Relative Humidity (RH) at 25°C) and with a flow rate of 100 mL min⁻¹) at 250°C for 18 hours, followed by a thermal treatment at 500°C for an additional 6 hours always under synthetic air. This step is essential to promote material crystallization and stabilization. Films deposited onto silicon substrates were also thermally treated using the same procedure. The pollutants were generated using permeation Teflon tubes placed inside controlled-temperature ovens. The initial concentrations of vapors were 157 ± 5 ppb for benzene, 288 ± 5 ppb for formaldehyde, and 408 ± 5 ppb for propanol.
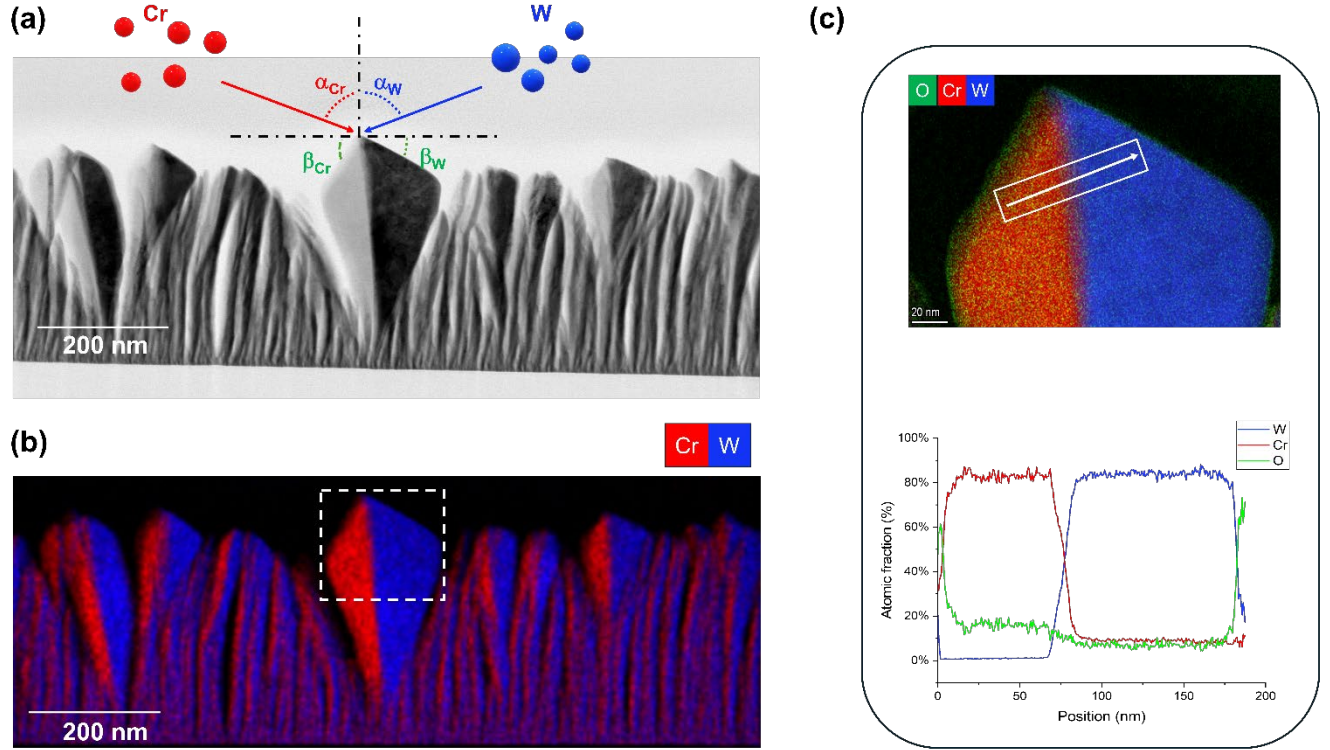
Figure 3: (a) Bright-field STEM image of the as-deposited film, (b) STEM-EDX elemental mapping, and (c) zoomed-in of the elemental map focused on a nanocolumn, along with the corresponding elemental composition analysis retrieved from the marked area. The white arrow shows the scan direction used for the elemental analysis.

The normalized response of the gas sensor was defined as $S = (R-R_0)/R_0$, where R is the sensor resistance in the presence of the pollutant (Ω) and R_0 is the resistance in pure synthetic air (Ω). A signal processing step was applied to the normalized response using a curve-fitting procedure implemented in Python, in order to smooth the data and enable accurate fitting. This step improved the signal-to-noise ratio, allowing a more precise evaluation of response amplitudes, especially at low analyte concentrations.

3   RESULTS AND DISCUSSION

### 3.1 Morphology, structure and composition of the W-Cr Janus thin film

To determine the optimal deposition conditions for getting a composition of approximately 50 at. % of each element, EDS analyses were conducted on films produced using different target currents. Figure 1 (b) illustrates the evolution of the composition by SEM-EDS of each element as a function of W and Cr target currents. To achieve a composition close to 50 at. % for each element, the current was set to 175 mA for the Cr target and 125 mA for the W target. Figure 2 reveals SEM top-views of the W-Cr film obtained with these deposition conditions (I_W = 125 mA and I_{Cr} = 175 mA), as-deposited and after the annealing treatment under synthetic air. As-deposited film's surface (Fig. 2 (a)) exhibits quadrilateral elongated-shapes perpendicular to the particle fluxes, with significant size heterogeneity, from *ca.* 5 to

ca. 250 nm. These shapes correspond to the tops of individual columns formed during the co-deposition of W and Cr. The elongation observed perpendicular to the W and Cr particle fluxes, commonly seen in GLAD films produced with a single source, is primarily attributed to shadowing asymmetry inherent to the GLAD process, especially significant for grazing angle > 70°.[50] This anisotropic microstructure results in the formation of distinct ridge-like features at the apex of the columns, arising from the oriented growth of both metal elements and contributing to notable surface roughness. The distinct contrast and separation between columns indicate shadowing effects during growth, consistent with a structure zone model (SZM) Type I regime.[51] Indeed, during the initial stage of growth, nucleation sites are formed randomly across the substrate surface. As columns evolve, they produce a shadowing effect that inhibits further growth in the shaded regions, leading to the extinction of some columns, which is particularly governed with the GLAD process. In addition, the dense columnar structure with minimal void spaces observed on the surface indicates the presence of surface porosity within the micro- to mesoporous range (*i.e.,* pores with diameters below 2 nm up to approximately 50 nm).
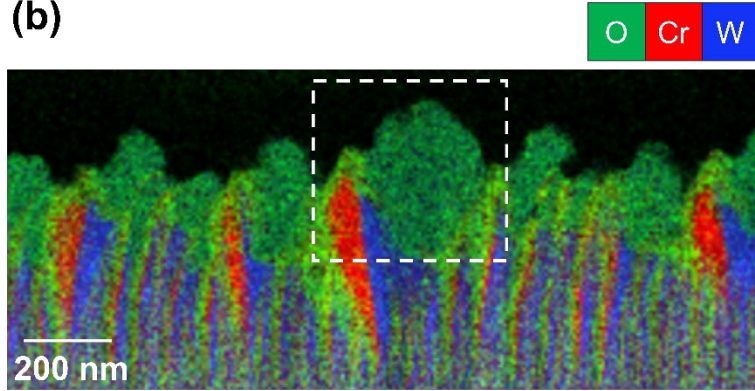
After annealing (Fig. 2 (b)), the film reveals a nanogranular texture with densely packed, near-spherical grains, with sizes ranging from *ca.* 10 to *ca.* 300 nm, uniformly distributed across the substrate.
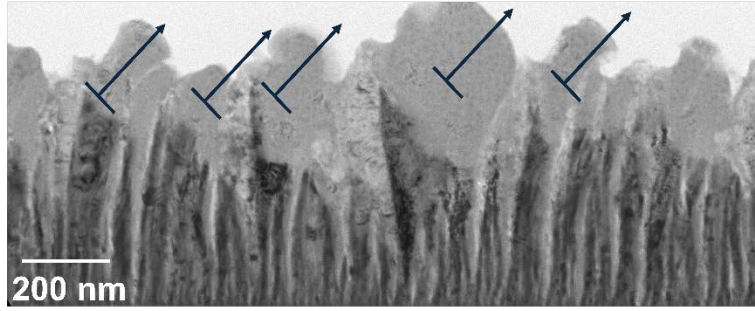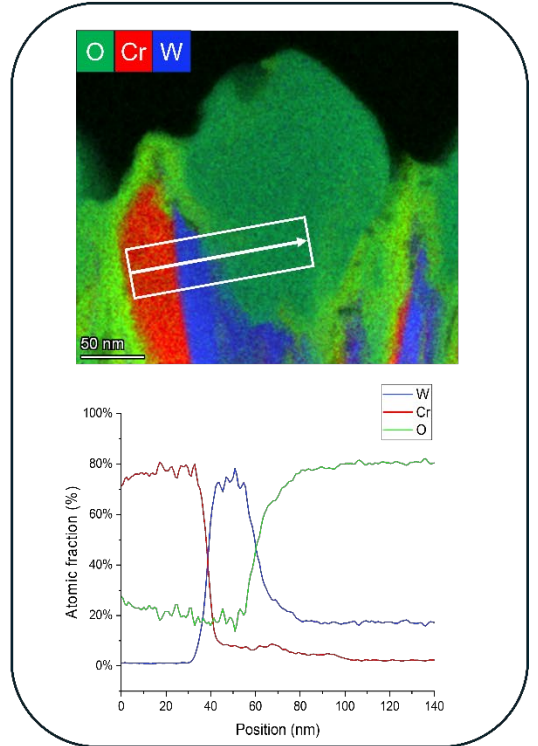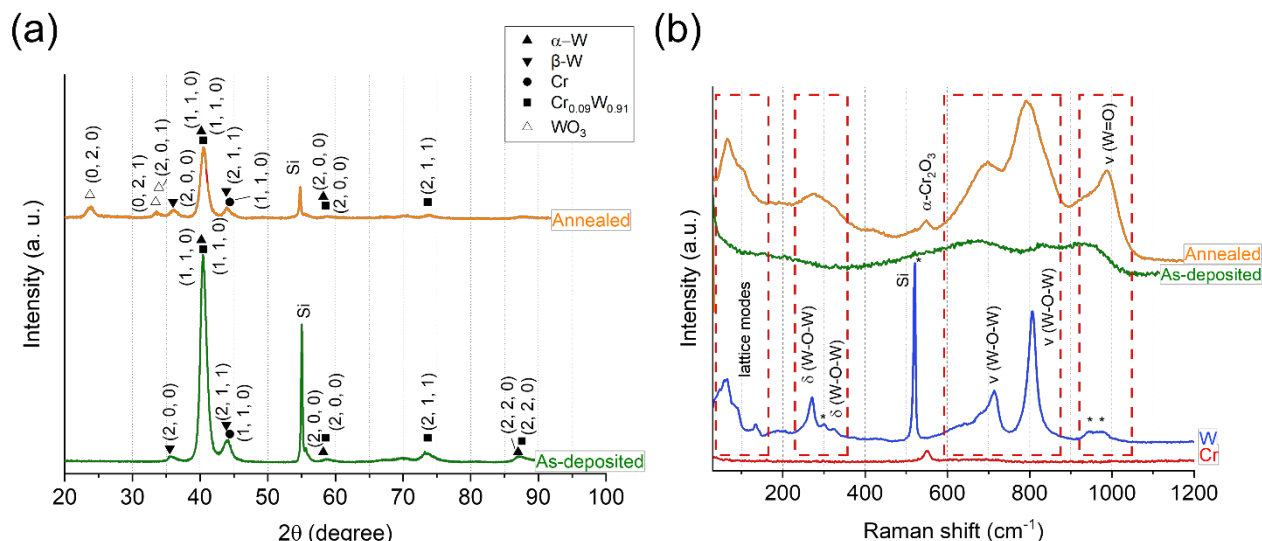
Figure 4: (a) Bright-field STEM image of the annealed film (arrows indicate the tungsten oxide growth), (b) STEM-EDX elemental mapping, and (c) zoomed-in of the elemental map focused on a nanocolumn, along with the corresponding elemental composition analysis retrieved from the marked area. The white arrow shows the scan direction used for the elemental analysis.

The apexes formed by the ridge-lines become less distinct, while the roughness remains significant and appears homogeneously distributed. The absence of large-scale defects or anisotropic features indicates uniform thermal energy distribution during the thermal treatment. Furthermore, the limited presence of voids on the annealed surface suggests that porosity remains largely unchanged by the annealing process.

To investigate in more detail the morphology and the elemental composition of these films, cross-sectional images were obtained using TEM, both before and after annealing at 500 °C. The bright-field STEM image of the as-deposited film (Fig. 3 (a)) reveals a film thickness close to 300 nm with a structure composed of vertically aligned, densely packed, and oriented wedge-shaped columns perpendicular to the substrate, confirming the film microstructure and texture in Zone I. The combination of columnar alignment and contrast variations strongly suggests that both targets contributed equally during the deposition. The images also highlight a pronounced heterogeneity in the nanocolumn growth, with larger columns appearing periodically along the substrate, a feature attributed to the shadowing effect previously discussed. As the columns grow in height, they expand progressively, resulting in a wedge-like cross-sectional morphology indicative of a faceted crystalline structure at the column apexes. The asymmetrical structure is closely related to the particle flux, which can be directly correlated to the trajectory regime of tungsten (W) and chromium (Cr) (Fig. 3 (a)). A detailed analysis of the angles between the facets and the theoretical trajectory of particles, denoted β_{Cr} and β_W, reveals that the angle associated with the tungsten flux is smaller than that observed for chromium, *i.e.*, $\beta_W < \beta_{Cr}$. Assuming a common initial deposition angle $\alpha = 80°$ for both materials, with respective target-to-substrate distances of 65 mm for W and 95 mm for Cr, and a background gas temperature of 300 K, the degree of thermalization can be evaluated. Considering the number of elastic collisions required for thermalization ($\eta = 9$ for W and $\eta = 3$ for Cr),[52, 53] the proportions of ballistic and thermalized atoms were estimated as a function of the sputtering pressure (Fig. S1 in Supporting Information (SI)). At a sputtering pressure of 0.27 Pa, approximately 55% of W atoms follow a ballistic trajectory, while about 58% of Cr atoms become thermalized due to the Ar background gas at 0.27 Pa and the Cr target-to-substrate of 95 mm. Consequently, tungsten tends to follow a more ballistic path, aligning more closely with the geometric deposition angle ($\alpha_W = 80°$). In contrast, chromium, subject to greater thermalization, displays a more diffuse particle flow, resulting in increased atomic scattering and a larger deviation between the facet angles and the theoretical geometric deposition trajectory (α_{Cr}).

The cross-sectional micrograph also reveals a voided architecture within the thin film, confirming the presence of well-developed porosity between and along the entire length of the nanocolumns.

Figure 5: (a) XRD patterns and (b) Raman spectra of Janus thin films as-deposited and after the annealing treatment. Asterisks indicate characteristic silicon peaks.

High-resolution transmission electron microscopy (HR-TEM) images taken from various regions within an isolated column (Fig. S2 (a) in SI) reveal that the chromium-rich side is predominantly amorphous, although a few small crystallites - averaging less than 10 nm in size - are still present, corresponding to the body-centered cubic (bcc) phase of chromium. In contrast, the tungsten-rich side of the nanocolumns appears to be more crystallized, as lattice planes corresponding to both the α- and β-phases of tungsten were identified. In the aforementioned figure, each HR-TEM micrograph is labeled with the zone axis (*i.e.*, lattice direction) along which the identified material is being observed under the microscope.

Janus nanocolumns are also confirmed by STEM-EDX measurements using atomic percentage maps (Fig. 3(b)), with one side composed of chromium and the other of tungsten. A small amount of native oxygen is detected at the surface of the nanocolumns, and the zoomed-in view in Fig. 3(c) reveals a well-defined interface between both elements. Figure 3(c) illustrates the distribution of W, Cr, and O within the column, based on counts collected from the entire outlined rectangle and along the indicated direction. The data reveal the presence of Cr (approximately 10 at. %) on the W-rich side of the Janus column. This observation suggests that Cr may have diffused across the interface, contributing to the formation of a distinct substitutional alloy, likely corresponding to Cr_xW_{1-x} with x ~ 0.1.

Figure 4 (a) shows the cross-sectional STEM image of the film after annealing in air at 250 °C for 18 hours, followed by an additional thermal treatment at 500 °C for 6 hours. The film's morphology undergoes significant changes, characterized by the formation of outgrowths primarily localized at the top of the nanocolumns and partially protruding from their right sides (see arrows in fig. 4 (a)). The overall film thickness increases by approximately 30% relative to its initial value, reaching up to 400 nm, mainly due to the development of these protrusions. Nevertheless, a closer examination of the image reveals that the thickness

of the nanocolumns themselves appears to remain unchanged. HR-TEM images taken from various regions within an isolated column, including the outgrowth (Fig. S2 (b) in SI), reveal that the α- and β-phases of tungsten as well as the bcc phase of chromium remain present in the bulk of the nanocolumn. Supplementary investigations further indicate that the outgrowths are composed primarily of amorphous tungsten oxide, with a few crystallites—measuring as small as 10 nm—corresponding to a distorted cubic phase of WO_3. The images were obtained at room temperature, and although the literature indicates that the orthorhombic phase is the most stable at 500 °C,[54] it is difficult to clearly identify this crystalline phase due to the very small crystallite size and the possibility of an allotropic transition occurring during cooling. Fig. 4 (b) shows an STEM-EDX atomic percentage map confirming that the Janus architecture is preserved as well as the clearly defined interface between both elements, even after the thermal treatment. It is also clear that the outgrowths are predominantly formed on the W side of the nanocolumns with the oxidation proceeding perpendicular to the tungsten facets (Fig. 4 (a)). An attempt to explain this behavior can be suggested using thermodynamic concepts, specifically the Gibbs energy-temperature diagram, commonly known as the Ellingham diagram. This diagram summarizes the relative thermodynamic stability of oxides as a function of the temperature. Figure S3 in SI presents the Ellingham diagram for W and Cr, from which it can be predicted that oxide formation occurs preferentially on tungsten rather than chromium. Indeed, a lower position on the diagram indicates a more negative standard free energy of formation, signifying greater oxide stability. In our case, the Ellingham diagram shows that the line for Cr_2O_3 is positioned lower than that for WO_3, indicating that Cr_2O_3 is the more stable oxide. This leads to the formation of a passivation layer on the chromium-rich side of the Janus nanocolumns, contributing to the stabilization of the oxide. The variation in elemental composition along a column over a distance of approximately 140 nm is shown in Fig. 4 (c). It can be noticed that the interface between both elements is

still preserved even after a thermal treatment higher than 500°C, and the outgrowths are predominantly composed of tungsten oxide. These hypotheses will be further supported by results from complementary analytical techniques presented in the following sections.

Figure 5 (a) displays the GIXRD patterns of the films recorded before and after the annealing treatment. As-deposited Janus film exhibits diffracted signal with peaks between 20 and 90°, which were labeled with the corresponding set of Miller indices. These peaks were attributed to the α- and β-phases of tungsten (PDF 00-073-0412 and PDF 00-047-1319, respectively) along with the bcc phase of metallic chromium (PDF 00-006-0694). Additionally, the presence of a Cr-substituted tungsten alloy ($Cr_{0.09}W_{0.91}$) was identified (PDF 04-020-5045), suggesting the diffusion of Cr atoms into the W-rich region of the Janus columns. These structural insights are consistent with the local atomic arrangements observed by STEM-EDX (Fig. 3 (d) and S2 (a)). After a thermal treatment at 500°C, the pattern of Janus film reveals new peaks which can be associated to WO_3 (PDF 01-073-6498). The broad peak widths, typically associated with small crystallite sizes, make it difficult to determine the exact nature of the phase. It is also interesting to note that the phases associated to pure metals (Cr and W) remain present in the thin film even after the annealing treatment. This finding confirms the TEM observations, showing that the main structure of the nanocolumns remained intact even after annealing at temperatures as high as 500 °C. No peaks of impurities were observed confirming the high purity of the as-prepared Janus thin film.

Further information on the crystal structure of the W-Cr Janus film sputtered onto (100) silicon substrate were obtained from Raman spectra. Figure 5 (b) presents the spectra of both the as-deposited and annealed W-Cr Janus films. For comparison, reference spectra of separately sputtered W and Cr films, each one annealed at 500 °C, are also shown. The spectrum of the annealed pure tungsten film exhibits the characteristic silicon substrate peak at around 520 cm^{-1}, along with several lower-intensity peaks identified with asterisks in Fig. 5 (b). This indicates that the excitation beam passes through the film and reaches the silicon substrate. In contrast, these peaks are not present in the spectra of the annealed pure chromium and W-Cr films, indicating that these films are opaque to the excitation laser. This confirms that the metallic chromium film is protected by a thin passivating oxide layer after annealing. In the case of the annealed W-Cr film, the results suggest the presence of sufficient metallic tungsten and chromium, which is consistent with previous TEM observations.

The spectrum of the as-deposited W-Cr film shows very weak and broad peaks, indicating surface oxidation of the deposited material forming an amorphous surface layer. The spectrum exhibits two bands centered around ~668 cm^{-1} and 844 cm^{-1}, attributed to stretching modes of W–O–W bonds,[55] along with another band near ~940 cm^{-1}, associated with the W^{6+}=O stretching mode of terminal oxygen atoms, which may be present on the film surface (*i.e.*, at the grain surface).[56]

For the annealed W-Cr film, the intensity of Raman signal is higher, and the bandwidth of individual bands is reduced compared to the as-deposited film. This suggests that the oxides formed in the annealed film are at least partially crystallized. In particular, the small peak observed at 548 cm^{-1} matches with the position of the peak observed for the annealed pure chromium film and identified as the A1g vibrational mode of α-Cr_2O_3.[57] This result is relevant, as it complements previous analyses.

Beyond the Cr_2O_3 peak, the Raman spectrum of the annealed W-Cr film shows strong similarity to that of the oxidized pure W film. However, the observed peak broadening and positional shifts indicate the presence of structural and/or compositional disorder in the annealed W-Cr film. In the low-frequency region, below 200 cm^{-1}, WO_3 lattice modes are clearly observed, as in the case of the annealed W film.[58] The distinct peaks at 275 and 326 cm^{-1} associated with W-O-W bending vibrations in monoclinic WO_3 become a broad band at 240-350 cm^{-1} for the annealed W-Cr film.[59] Literature reports associate the disappearance of the 325 cm^{-1} peak with a significant presence of oxygen vacancies.[60]

At higher frequencies, the spectrum of the annealed W film shows the main peaks characteristic of monoclinic WO_3 at 714 and 806 cm^{-1}, which are assigned to W–O–W stretching vibrations.[61, 62] These peaks are broadened and slightly shifted to lower frequencies for the annealed W-Cr film, suggesting structural disorder likely induced by the presence of chromium.

In the 900-1100 cm^{-1} range, the spectrum of the annealed W-Cr film displays a prominent band, in contrast to the annealed W film, which shows only low-intensity peaks originating from the Si substrate. The broadband observed at ~940 cm^{-1} for the as-deposited W-Cr film, assigned to stretching vibrations of W^{6+}=O terminal oxygen atoms,[56, 59] is still present for the annealed W-Cr film, accompanied by the appearance of a narrower peak at 987 cm^{-1}. According to the literature, the intensity and the position of the W^{6+}=O peak is influenced by crystallite size, increasing as the crystallite size decreases.[63] This observation is consistent with previous TEM and XRD analysis, which indicated crystallites as small as 10 nm.

In summary, these spectral analyses confirm that the annealed W-Cr film mostly consists of tungsten oxide, and that the nearby presence of chromium induces structural disorder. As described previously, in the Janus configuration, oxidation is confined to the edges of the nanocolumns, resulting in a continuous protective oxide shell surrounding the metallic nanostructures.
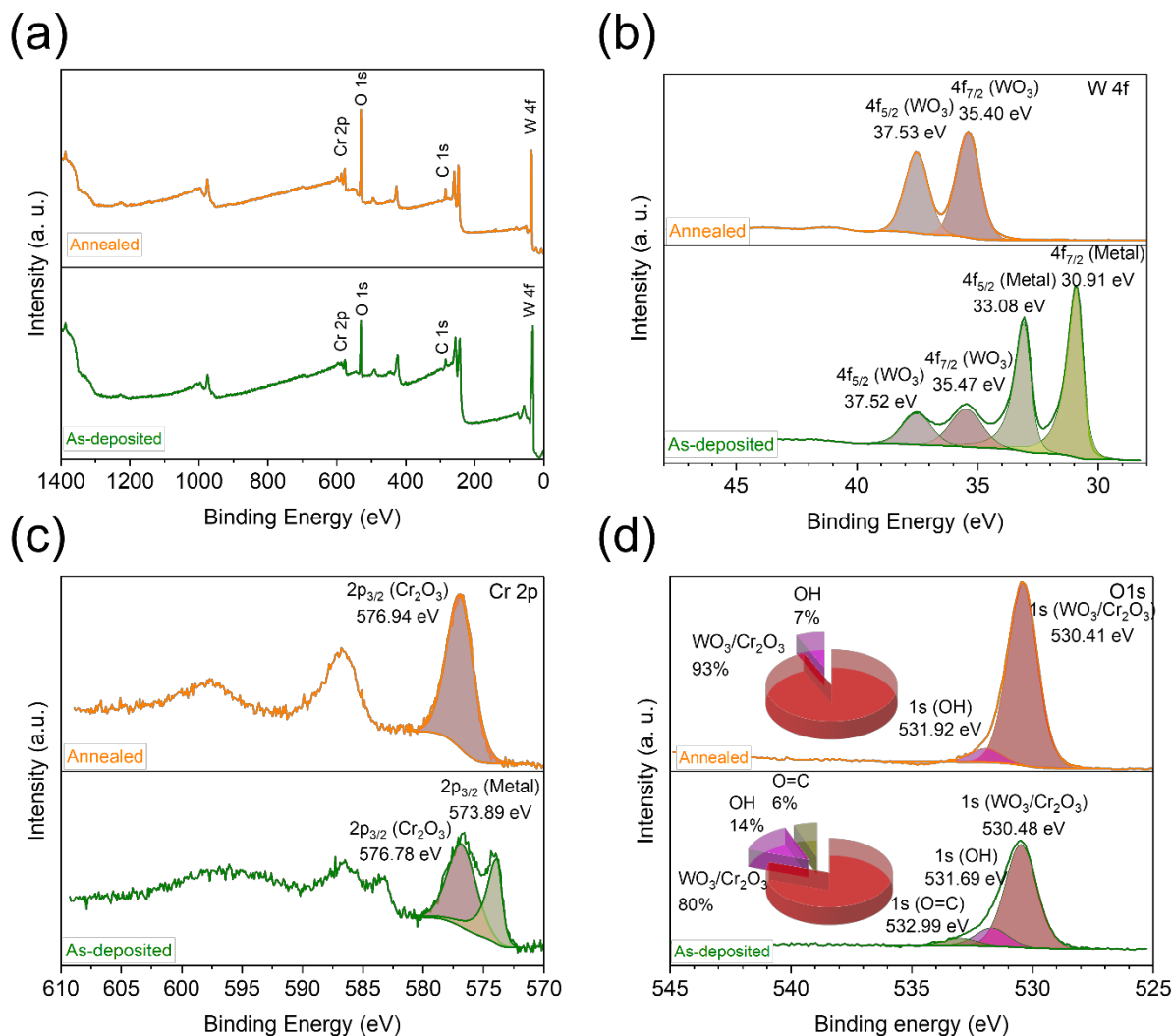
Figure 6: (a) XPS survey spectra of W-Cr Janus thin film as-deposited and after the annealing treatment. High-resolution XPS spectra of (b) W 4f, (c) Cr 2p, and (d) O 1s of the of W-Cr Janus thin film as-deposited and after the annealing treatment.

To complete these analyses, XPS studies were also performed to get information on the surface chemistry (chemical bonding and defect states) of Janus thin film samples, as-deposited and after annealing at 500°C. The complete measured spectra for each sample, presented in Fig. 6 (a), appear nearly identical. However, a focus on the W 4f and Cr 2p core lines decomposition reveals important differences between as-deposited and annealed film (Fig. 6 (b) and (c)). In the as-deposited film, two W 4f doublets are observed at binding energies of 30.91 and 33.08 eV, corresponding to the W $4f_{7/2}$ and W $4f_{5/2}$ states of metallic W^0, and at 35.47 and 37.52 eV, attributed to W^{6+} in WO_3.

After thermal treatment, only the typical doublet associated with W^{6+} in WO_3, at 35.40 and 37.53 eV, remains detectable, indicating the disappearance of the metallic tungsten component at the surface of the film. Similar observations can be made for the Cr 2p region where the as-deposited film exhibit Cr $2p_{1/2}$ and Cr $2p_{3/2}$ states essentially build-up of metallic Cr^0 and Cr^{3+} in Cr_2O_3. Following the annealing treatment, only the contribution of Cr^{3+} in Cr_2O_3 is identified in the Cr $2p_{1/2}$ and Cr $2p_{3/2}$ states. These observations

confirm that, prior to annealing in air, the surface consists of metallic Cr and W, along with a thin metal oxide layer. After annealing at 500°C, the surface becomes fully oxidized, with no detectable presence of metallic elements.

The high-resolution spectra of O 1s, represented in Fig. 6 (d), are categorized into two types of oxygen species: Lattice oxygen (O_L) corresponding to ions directly connected to metal cations (Cr^{3+} and W^{6+}) and chemisorbed oxygen (O_C) associating to species resulting to the adsorption, at the near surface of material, of atmospheric water and CO/CO_2 from the ambient air. The oxygen species and their contents, derived from peak intensities, are illustrated in the pie charts in Fig. 6 (d). It is worth noting that the contribution of the O=C binding disappears after the thermal treatment at 500°C.

This physico-chemical characterization provided a deeper understanding of the morphology, structure, and chemical composition of the W-Cr Janus structure. Subsequently, the annealed W-Cr Janus film was employed as a sensitive layer for the detection of various volatile organic compounds in air.
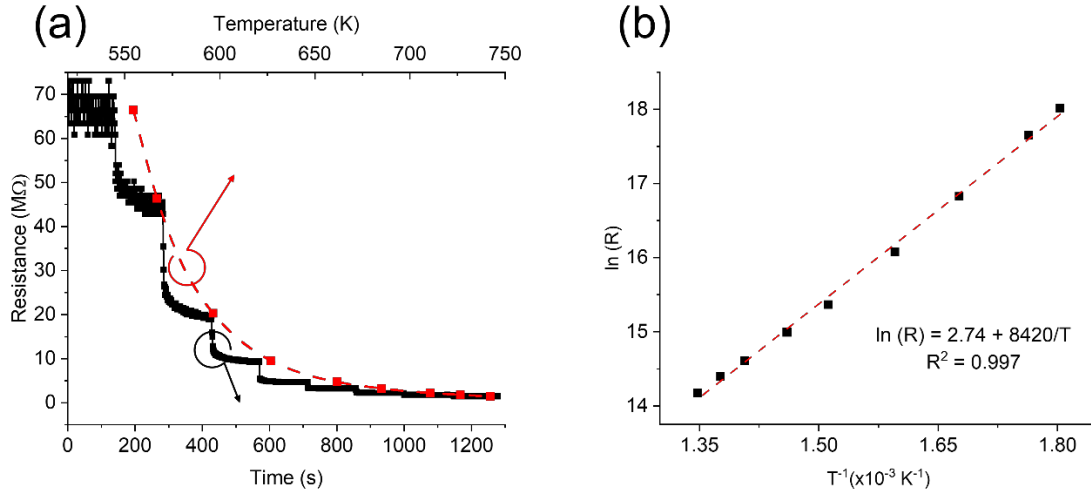
Figure 7: (a) Dynamic resistance variation of the annealed W-Cr Janus thin film as the temperature increases from 281 to 469 °C (black line) and evolution of the R values, measured when the resistance is stable at a given temperature, plotted as a function of temperature (red dashed curve). (b) Arrhenius plot showing ln(R) vs. the inverse temperature (T⁻¹) for the W-Cr Janus thin film.

3.2 Sensing performance

Before conducting sensing tests under pollutants, the stability and the charge transport mechanism within the Janus film were explored by recording the evolution of the dynamic resistance variation with temperature interval as a function of time in synthetic air. From Fig. 7 (a) it can be noticed that the annealed W-Cr Janus film is thermally ultrasensitive, with resistance decreasing from around 6.65×10^7 Ω at ~280°C to 1.43×10^6 Ω at ~470°C. Below 280°C, the film's resistance is too high to be measured using a conventional setup. Based on the dynamic resistance variation with temperature interval, the curve of resistance (measured when the resistance is stable and before each temperature increment) as a function of temperature can be plotted (red dashed line in Fig. 7 (a)). This curve exhibits a nonlinear decrease of resistance with increasing temperature, consistent with Arrhenius behavior dominated by thermal activation, as described in Equation (1).

This trend is characteristic of semiconducting materials.

$$R(T) = R_0 \exp\left(E_a/k_B T\right) \tag{1}$$

E_a is the activation energy and k_B is the Boltzmann constant (8.62×10^{-5} eV.K⁻¹).

The activation energy E_a (eV) of the material can be obtained from the fitted linear Arrhenius plot of the logarithm of the resistance ln(R) *vs.* the reciprocal temperature T^{-1} shown in Figure 7 (b), following Equation (2).

$$\ln(R) = \ln(R_0) + E_a/k_B T \tag{2}$$

For the annealed W-Cr Janus structure, the activation energy was calculated to be 726 ± 10 meV, which is consistent with values reported in the literature for semiconducting materials, typically ranging from 50 to 860 meV.[64] As commonly suggested by several authors, the Schottky barrier - associated with the potential barrier formed at grain boundaries - can be approximated by the determined activation energy.[65] For our thin film, the presence of high intergranular potential barriers significantly limits the mobility of charge carriers within the material, resulting in high resistance under air.
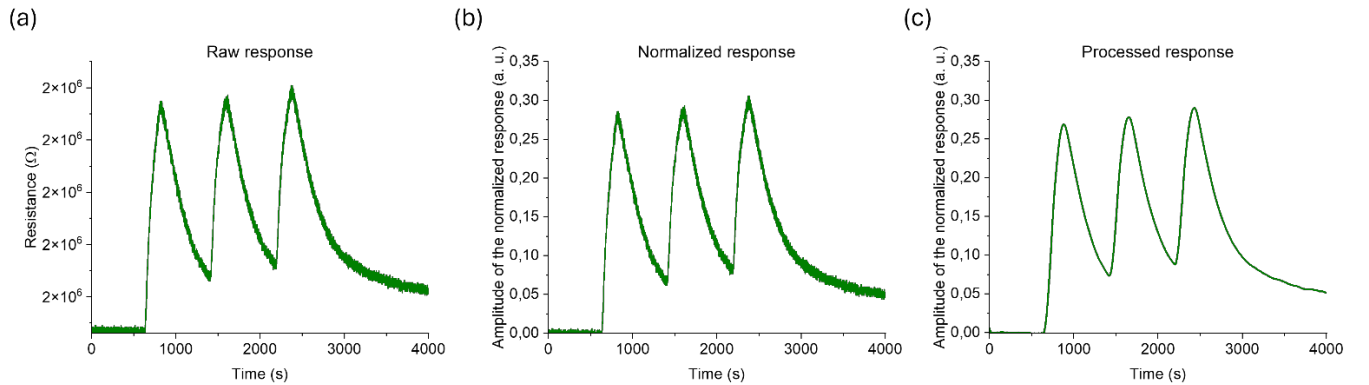
Figure 8: Example of a dynamic sensing transient recorded during the detection of 408 ± 5 ppb of propanol at 450 °C: (a) raw signal, (b) after normalization, and (c) after signal processing.
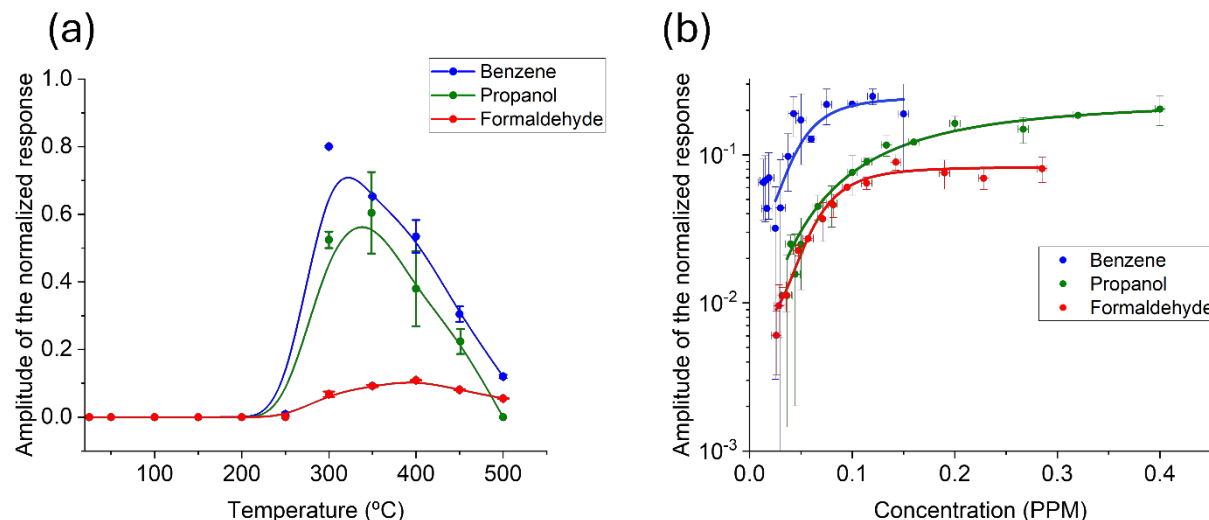
Figure 9: (a) Evolution of the normalized response amplitude as a function of the sensitive surface temperature. (b) Amplitude of the normalized response as a function of the pollutant concentrations.

After these first experiments under air flow, the gas sensing performances of the annealed W-Cr Janus film were investigated with three different indoor air pollutants, *i.e.*, benzene, formaldehyde and propanol. It is admitted that the gas sensing properties of MOS gas sensors are significantly affected by the sensing layer's temperature. Fig. 8 shows an example of the resistance variation for propanol detection at 450 °C before and after signal processing, while Fig. S4 in SI presents several sequences illustrating the evolution of the annealed W-Cr Janus sensor resistance at different operating temperatures under exposure to benzene, formaldehyde, and propanol. Pollutant concentrations were equal to 157±5 ppb, 288±5 ppb, and 408±5 ppb for benzene, formaldehyde and propanol, respectively. Each pollutant exposure lasted for 3 minutes, followed by a 10-minute recovery period under synthetic air flow. This sequence was repeated three times to enable statistical analysis (*e.g.*, error bars). When changing the operating temperature, a slight baseline drift and variations in signal amplitude can be observed. These effects may be attributed to the long stabilization time required by the sensor, as well as the chemical nature of the pollutant, which can require more time to completely desorb from the sensitive surface. It is interesting to note that the annealed W-Cr Janus thin film exhibits a p-type behavior since the resistance increase when exposed to a reducing gas. Based on the previously described physico-chemical characterization, it can be concluded that the structures are primarily composed of Cr_2O_3 and WO_3 after the annealing treatment, which are p-type and n-type metal oxide semiconductors, respectively. In our case, the electrical response measurements suggest that Cr_2O_3 predominantly governs the overall semiconducting behavior of the gas sensor.

It is possible to evaluate the optimized temperatures for the detection of benzene, formaldehyde, and propanol by plotting the average amplitude of the normalized response (S), after a signal processing, as a function of the sensitive layer temperature (Fig. 9 (a)). As is typically observed with resistive gas sensors, the optimal operating temperatures differed slightly for each target pollutant and were determined to be 300, 400, and 350 °C for benzene, formaldehyde, and propanol, respectively. It is noteworthy that the gas sensor does not exhibit any resistance variation under pollutants below 250 °C. Figure S5 in Supporting Information shows the long-term exposure sequence obtained for the detection of various concentrations of each pollutant. Each pollutant concentration was chosen randomly and replicated at least two times to assess both the repeatability and the long-term stability of the sensor. For each pollutant, these sequences represent more than six hours of continuous acquisition under alternating air and pollutant exposures. Each sequence was replicated three times, representing approximately one month of experiments, including all pollutants. The W-Cr sensor demonstrates an excellent repeatability and long-term stability across all tested pollutants, as the response amplitudes consistently correlate with the corresponding concentrations. Fig. 9 (b) depicts the calibration curves for each pollutant at their optimized sensing temperature. As expected, these calibration curves consist of a dynamic linear region, where the concentration is directly proportional to the sensor response, followed by a plateau that can be attributed to the saturation of the sensitive surface. The detection limit is defined as the minimum concentration at which pollutants can be reliably identified. In this study, we estimated the detection limit from the dilution curves as the concentration corresponding to a signal-to-noise ratio of 3 (S/N = 3). After the smoothing step (see Fig. 8 (c) and Fig. S5 in SI), the average noise was significantly reduced and estimated to be approximately 0,054, 0,002 and 0,008 for benzene, formaldehyde and propanol sensing tests, respectively. For each pollutant, the detection limit was estimated to be approximately 37 ± 5, 26 ± 5, and 36 ± 5 ppb for benzene, formaldehyde, and propanol, respectively. These values comply with the permissible short-term exposure limits for inhalation of these compounds.
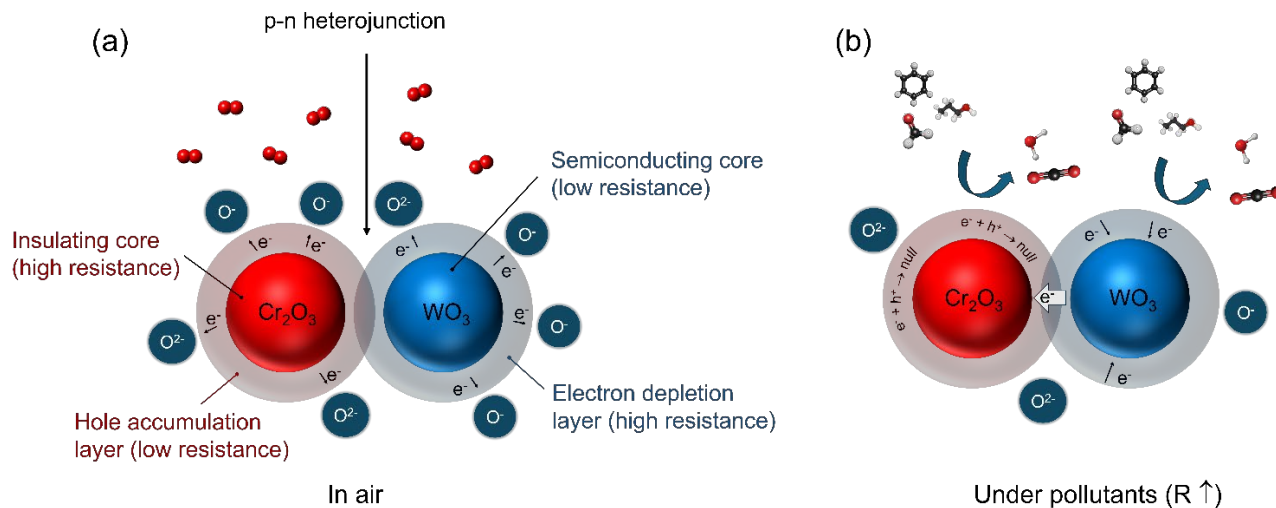
Figure 10: Schematic illustration of gas-sensing mechanism of the Cr_2O_3–WO_3 heterojunction: (a) Under air exposure, an electron depletion layer (EDL) and a hole accumulation layer (HAL) are formed at the surface of WO_3 and Cr_2O_3 particles; (b) Upon exposure to pollutant gases, adsorption on ionosorbed oxygen species near the surface of WO_3 and Cr_2O_3 induces electron transfer, followed by electron capture by holes.
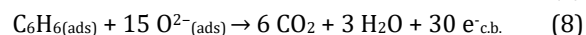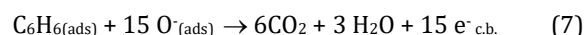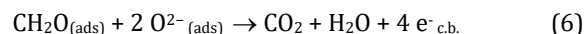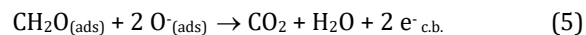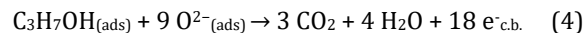
3.3 Influence of humidity

Under real-world conditions, humidity is a well-known interfering factor for chemical gas sensors and can reach levels as high as 60% RH at 25 °C. Fig. S6 in the Supplementary Information presents preliminary experiments for propanol detection under varying humidity levels, from 8% to 60% RH at 25 °C. This figure clearly shows that even at a very low humidity level (*i.e.*, 8% RH at 25 °C), water has a strong influence on the sensing response of the annealed W–Cr Janus film. Specifically, the amplitude of the response decreases compared to measurements performed in nearly dry air (2% RH at 25°C). The competitive adsorption of water and propanol molecules on the surface of the nanostructured Janus material during detection significantly affects the sensor's performance toward propanol. Up to 45% RH at 25 °C, it remains possible to detect 102 ± 5 ppb of propanol, which is still within the permissible short-term exposure limit. However, above this humidity level, the sensor signal becomes too strongly affected by water to clearly identify the presence of propanol. It is worth noting that the baseline level of the sensor varies directly with the relative humidity and exhibits good repeatability.

3.4 A possible gas sensing mechanisms

Although various interaction mechanisms can occur between a metal oxide surface and gas molecules, the literature generally agrees that variations in the material's resistance are primarily explained by electronic conductivity mechanisms involving adsorbed oxygen species at the surface. In our case, the gas-sensing mechanism of the W–Cr Janus sensor can be interpreted based on the well-established space-charge layer model describing the interface of a p–n heterojunction.[66-67] In the as-elaborated composite material, Cr_2O_3 is a p-type MOS with a reported work function and electron affinity equal to 5.9 eV and 3.76 eV, respectively, while WO_3 is a n-type MOS with work function and electron

affinity equal to 4.8 eV and 3.94 eV, respectively.[66] Based on these values, a schematic diagram of the band gap structure (Figure S7 in SI) and gas sensing mechanism can be proposed. Due to the difference in work function, electrons transfer from WO_3 (which has a higher Fermi level) to Cr_2O_3 (with a lower Fermi level) until equilibrium is achieved, as illustrated in Fig. S7 in SI. When exposed to air, oxygen molecules adsorb onto the surface of the material and capture free electrons from both WO_3 and Cr_2O_3 particles. This process leads to the formation of an electron depletion layer (EDL) and a hole accumulation layer (HAL) at the shell of the WO_3 and Cr_2O_3 particles, respectively, thereby establishing a p-n heterojunction at the interface (Fig. 10 (a)). Gas sensing results indicate that the annealed W–Cr Janus material exhibits p-type MOS behavior, characterized by an increase in resistance when exposed to reducing gases. This implies that the overall conductance is mainly controlled by holes in the outer shell layer, which act as the majority carriers.

When exposed to electron-donating gases (*e.g.*, benzene, formaldehyde, and propanol), these gases react with the ionosorbed oxygen species near the surface of WO_3 and Cr_2O_3 particles. The overall mechanisms describing the gas–solid interactions involved in the sensing process are complex; however, a few representative reactions can be outlined as follows:

$$C_3H_7OH_{(ads)} + 9\ O^-_{(ads)} \rightarrow 3CO_2 + 4\ H_2O + 9\ e^-_{c.b.} \quad (3)$$

$$C_3H_7OH_{(ads)} + 9\ O^{2-}_{(ads)} \rightarrow 3\ CO_2 + 4\ H_2O + 18\ e^-_{c.b.} \quad (4)$$

$$CH_2O_{(ads)} + 2\ O^-_{(ads)} \rightarrow CO_2 + H_2O + 2\ e^-_{c.b.} \quad (5)$$

$$CH_2O_{(ads)} + 2\ O^{2-}_{(ads)} \rightarrow CO_2 + H_2O + 4\ e^-_{c.b.} \quad (6)$$

$$C_6H_6_{(ads)} + 15\ O^-_{(ads)} \rightarrow 6CO_2 + 3\ H_2O + 15\ e^-_{c.b.} \quad (7)$$

$$C_6H_6_{(ads)} + 15\ O^{2-}_{(ads)} \rightarrow 6\ CO_2 + 3\ H_2O + 30\ e^-_{c.b.} \quad (8)$$

The oxidation reactions release electrons into the conduction band (c.b.) of both Cr_2O_3 and WO_3 materials, which subsequently recombine with holes in the hole accumulation layer (Fig. 10 (b)). This recombination reduces the hole concentration, leading to an increase of the oxidized W-Cr Janus material's resistance (*i.e.*, a decrease of the conductance) since holes are the charge carriers. An increased electron transfer to the material enhances electron–hole recombination, resulting in a larger variation in resistance. According to Eqs. (3)–(8), the reaction of benzene with the sensitive surface induces the highest electron transfer, which may explain its higher response compared to the other pollutants.

Since the literature does not report any study on the development of W–Cr Janus structures for air pollutant detection, a direct comparison is challenging. Nevertheless, some investigations have explored Cr-doped WO_3 for the detection of VOCs, formaldehyde, and alcohol vapors, providing relevant reference points.[66, 68-70] Table 1 in Supporting Information reports on a non-exhaustive selection of studies utilizing Cr and W in the design of sensitive materials made of heterojunctions. We notice that the used of the GLAD co-sputtering method for thin film growth yields significantly better results in term of sensitivity to VOCs of the same family compared to the current state of the art.

4 CONCLUSION

In this study, we reported on the elaboration of nanostructured W-Cr Janus heterojunction thin films using GLAD process in reactive co-sputtering mode and demonstrated their ability to detect various indoor air pollutants, at the ppb level. Electron microscopy investigations revealed the formation of vertically aligned and well-organized W-Cr columns with distinct interfaces, preserved even after annealing at temperatures as high as 500 °C. Annealing treatment of the film leads to the formation of a superficial oxide layer that envelops the Janus nanocolumns, accompanied by the emergence of outgrowths predominantly on the W-rich side of the columns. Crystallographic analysis of the W-rich region of the Janus nanocolumns revealed the coexistence of multiple tungsten phases (α and β), along with a Cr-substituted tungsten alloy (*i.e.*, $Cr_{0.09}W_{0.91}$), resulting from slight chromium diffusion during deposition. Outgrowths observed on the W-side surface after the thermal treatment were primarily composed of distorted cubic WO_3. On the other hand, the bulk of the Cr-rich region is mainly amorphous, whereas the superficial oxide layer is composed of α-Cr_2O_3.

Electrical measurements revealed a p-type behavior of the film, despite the fact that WO_3 and Cr_2O_3 compounds are typically associated with n-type and p-type conductivity, respectively. The developed Janus heterojunctions not only demonstrate excellent stability and repeatability as VOC sensors, but also highly promising sensitivity with detection limits of 37 ± 5 ppb for benzene, 26 ± 5 ppb for formaldehyde, and 36 ± 5 ppb for propanol were achieved in nearly dry air.

Further studies will address a broader set of indoor air interferents, including ammonia, toluene and xylene, as well as investigations about alternative Janus nanostructures based on diverse material compositions. The integration of multiple Janus nanostructures on a single sensor platform will enable the design of matrix-type sensor systems capable of obtaining a chemical signature of complex environments.

This work paves the way for future innovative materials in pollutant detection technologies, where the design of Janus nanocolumns with carefully selected components could lead to major breakthroughs in environmental sensing.

ASSOCIATED CONTENT

The Supporting Information is available free of charge at:
Figure S1: Proportion of ballistic and thermalized Cr and W atoms in Ar as a function of argon pressure: Figure S2: HR-TEM micrographs of the W-Cr Janus thin film as-deposited and after an annealing treatment; Figure S3: Ellingham diagram comparing the thermodynamic stability of WO_3 and Cr_2O_3; Figure S4: Dynamic sensing transients for each pollutant at different sensing temperatures; Figure S5: Long-term exposure sequences of the sensor to various concentrations of pollutants; Figure S6: Dynamic sensing transients for various relative humidity; Figure S7: Schematic illustration of the band gap structure of the W–Cr Janus gas sensor.

AUTHOR INFORMATION

Corresponding Author

* Jean-Baptiste Sanchez – Université Marie et Louis Pasteur, CNRS, Institut FEMTO-ST, F 25000, Besancon, France; orcid.org/0000-0002-3303-0973; Phone: +33 3 63 08 24 93; Email: jbsanche@femto-st.fr

Present Addresses

†If an author's address is different than the one given in the affiliation line, this information may be included here.

Author Contributions

G.V.S. performed the thin film deposition, electronic images acquisition, VOCs detection experiments, analyzed the data and designed the figures. H.G. performed the thin film deposition, A.K., O.H., N.G., R.S., J.J.J., M.D.C.M.D.L., A. J. S. and F. M. M. carried out the physico-chemical analysis, A.B., N.M. and V.P analyzed the data and provided expertise and feedback, J.-B.S. conceived the presented idea, analyzed the data, and took the lead in writing the manuscript. All authors contributed to the interpretation of the results, discussion, and writing of the manuscript. All authors gave their approval to the final version of the manuscript.

REFERENCES

[1] Dey A. Semiconductor metal oxide gas sensors: A review. *Mater. Sci. Eng. B* **2018**, 229, 206-217.

[2] Nascimento E.P.; Firmino H.C.T.; Neves G.A.; Menezes R.R. A review of recent developments in tin dioxide nanostructured materials for gas sensors. *Ceram. Int.* **2022**, 48 (6), 7405-7440.

[3] Sun Y.-F.; Liu S.-B.; Meng F.-L.; Liu J.-Y.; Jin Z.; Kong L.-T.; Liu J.-H. Metal oxide nanostructures and their gas sensing properties: A Review. *Sensors* **2012**, 12, 2610-2631.

[4] Ji H.; Zeng W.; Li Y. Gas sensing mechanisms of metal oxide semiconductors: A focus review. *Nanoscale* **2019**, 11, 22664–22684.

[5] Mirzaei A.; Ansari H. R.; Shahbaz M.; Kim J.-Y.; Kim H. W.; Kim S. S. Metal oxide semiconductor nanostructure gas sensors with different morphologies. *Chemosensors* **2022**, 10 (7), 289-312.

[6] Goel N.; Kunal K.; Kushwaha A.; Kumar M. Metal oxide semiconductors for gas sensing. *Engineering Reports* **2023**, 5:e12604.

[7] Krishna K. G.; Parne S.; Pothukanuri N.; Kathirvelu V.; Gandi S.; Joshi D. Nanostructured metal oxide semiconductor-based gas sensors: A comprehensive review. *Sens. Actuator A-Phys.* **2022**, 341, 113578.

[8] Byakodi M.; Shrikrishna N. S.; Sharma R.; Bhansali S.; Mishra Y.; Kaushik A.; Gandhi S. Emerging 0D, 1D, 2D, and 3D nanostructures for efficient point-of-care biosensing. *Biosens Bioelectron.* **2022**, 12, 100284.

[9] Karmakar S.; Sett A; Maity P. C.; Sha R.; Bhattacharyya T. K.; Lahiri I. A highly selective room-temperature formaldehyde gas sensor based on vertically aligned 1D NiCo2O4 nanoneedles. *Mater. Lett.* **2023**, 350, 134927.

[10] Jang Y.-W.; Jo J.-W.; Park S. K.; Kim J. Room-temperature gas sensors based on low-dimensional nanomaterials. *J. Mater. Chem. C* **2024**,12, 18609-18627.

[11] Bisht S.; Dhariwal N.; Yadav P.; Chahar M.; Singh D.; Kumar V. Unveiling the impact of 2-D materials on the gas sensing properties of metal oxides: A review. *J. Environ. Chem. Eng.* **2025**, 13 (2), 115980.

[12] Prakash C.; Yadav A. K.; Sharma M.; Singh V. K.; Dixit A. Recent developments on 2D-materials for gas sensing application, *J. Phys. Condens. Matter.* **2024**, 37, 193004.

[13] Degler D.; Weimar U.; Barsan N. Current understanding of the fundamental mechanisms of doped and loaded semiconducting metal-oxide-based gas sensing materials, *ACS Sens.* **2019**, 4 (9), 2228–2249.

[14] Zhu L.-Y.; Ou L.-X.; Mao L.-W.; Wu X.-Y.; Liu Y.-P.; Lu H.-L. Advances in noble metal-decorated metal oxide nanomaterials for chemiresistive gas sensors: Overview. *Nano-Micro Lett.* **2023**, 15, No. 89.

[15] Uma S., Shobana M.K., Band structure and mechanism of semiconductor metal oxide heterojunction gas sensor, *Inorg. Chem. Commun.* **2024**, 160, 111941.

[16] Yang S.; Lei G.; Xu H.; Lan Z.; Wang Z.; Gu H. Metal Oxide Based heterojunctions for gas sensors: A Review. *Nanomaterials* **2021**, 11 (4), 1026.

[17] Miller D. R.; Akbar S. A.; Morris P. A. Nanoscale metal oxide-based heterojunctions for gas sensing: A review., *Sens. Actuator B-Chem.* **2014**, 204, 250-272.

[18] He T.; Liu W.; Lv T.; Ma M.; Liu Z.; Vasiliev A.; Li X. MXene/SnO2 heterojunction based chemical gas sensors, *Sens. Actuator B-Chem.* **2021**, 329,129275.

[19] Wang Q.; Kou X.; Liu C.; Zhao L.; Lin T.; Liu F.; Yang X.; Lin J.; Lu G. Hydrothermal synthesis of hierarchical CoO/SnO2 nanostructures for ethanol gas sensor. *J. Colloid. Interf.* **2018**, 513, 760-766.

[20] Chen Y.; Cao Y. Ultrasensitive and low detection limit of acetone gas sensor based on ZnO/SnO2 thick films, *RSC Adv.* **2020**, 10, 35958-35965.

[21] Yang B.; Song Y.; Song Y.; Ma Z.; Sun J. TiO2 QDs/MoSe2 heterojunctions for enhanced photo-excited charge separation and gas sensing performance, *Sens. Actuator B-Chem.* **2023**, 379, 133124.

[22] Katti V.R.; Debnath A.K.; Muthe K.P.; Kaur M.; Dua A.K.; Gadkari S.C.; Gupta S.K.; Sahni V.C. Mechanism of drifts in H2S sensing properties of SnO2:CuO composite thin film sensors prepared by thermal evaporation, *Sens. Actuators B Chem.* **2003**, 96, 245–252.

[23] Song X.; Li L.; Chen X.; Xu Q.; Song B.; Pan Z.; Liu Y.; Juan F.; Xu F.; Cao B. Enhanced triethylamine sensing performance of A-Fe2O3 nanoparticle/ZnO nanorod heterostructures, *Sens. Actuators B-Chem.* **2019**, 298, 126917.

[24] Brett M. J.; Seto M. W.; Sit J. C.; Harris K. D.; Vick D.; Robbie K. Glancing angle deposition: Recent research results, Proc. SPIE 3790, *Engineered Nanostructural Films and Materials.* **1999**, 114-118.

[25] Hawkeye M. M.; Brett, M. J. Glancing angle deposition: Fabrication, properties, and applications of micro- and nanostructured thin films. *J. Vac. Sci. Technol. A.* **2007**, 25, 1317.

[26] Barranco A.; Borras A.; Gonzalez-Elipe A. R.; Palmero A. Perspectives on oblique angle deposition of thin films: From fundamentals to devices. *Prog Mater Sci.* **2016**, 76, 59-153.

[27] Robbie K.; Beydaghyan G.; Brown T., Dean C.; Adams J.; Buzea C. Ultrahigh vacuum glancing angle deposition system for thin films with controlled three-dimensional nanoscale structure. *Rev. Sci. Instrum.* **2004**, 75, 1089.

[28] Zhou C.; Gall D. Two-component nanorod arrays by glancing-angle deposition. *Small* **2008**, 4, No. 9, 1351–1354.

[29] Motemani Y.; Khare C.; Savan A.; Hans M.; Paulsen A.; Frenzel J.; Ludwig, A. Nanostructured Ti–Ta thin films synthesized by combinatorial glancing angle sputter deposition. *Nanotechnology* **2016**, 27 (49), 495604.

[30] Ye Y.; Luan J.; Wang M.; Chen Y.; Wilson D. A.; Peng F.; Tu Y. Fabrication of self-propelled micro- and nanomotors based on Janus structures. *Chem. Eur. J.* **2019**, 25, 1-19.

[31] Zhou C.M.; Li H.F.; Gall D. Multi-component nanostructure design by atomic shadowing, *Thin Solid Films* **2008**, 517, 1214-1218.

[32] Pedrosa P.; Ferreira A.; Martin N.; Arab Pour Yazdi M.; Billard A.; Lanceros-Méndez S.; Vaz F. Nano-sculptured Janus-like TiAg thin films obliquely deposited by GLAD co-sputtering for temperature sensing. *Nanotechnology* **2008**, 29, 355706.

[33] Jinsong Y. H.; Zhao W. Y. Designing catalytic nanomotors by dynamic shadowing growth. *Nano Lett.* **2007**, 7, 5, 1369–1375.

[34] Hu Z.; Li S.; Li F.; Wang T.; Shao H.; Dong X. Rational design of ZnO-SnO2 Janus nanofibers for highly sensitive triethylamine detection. *Sens. Actuator B-Chem.* **2025**, 423, 136805.

[35] Wang R.; Lan K.; Chen Z.; Zhang X.; Hung C.-T.; Zhang W.; Wang C.; Wang S.; Chen A.; Li W.; Xu X.; Zhao D. Janus mesoporous sensor devices for simultaneous multivariable gases detection. *Matter* **2019**, 1 (5), 1274-1284.

[36] Jiang J.; Pi Q.; Zhou J.; Du Y.; Li Y. A simple preparation of ultrathin AuNWs-PEDOT:PSS bilayer Janus film for high performance chemiresistive ammonia gas sensor. *Sens. Actuator B-Chem.* **2023**, 394, 134370.

[37] Jin C.; Tang X.; Tan X.; Smith S. C.; Dai Y.; Kou L. Janus MoSSe monolayer: A superior and strain-sensitive gas sensing material. *J. Mater. Chem. A* **2019**, 7, 112049.

[38] Singh D.; Ahuja R. Highly sensitive gas sensing material for environmentally toxic gases based on Janus NbSeTe monolayer. *Nanomaterials* **2020**, 10, 2554.

[39] Kopar A. S.; Coşkun A.; Özerbaş Z. E.; Küçük B. A.; Turalıoğlu K.; Çoban Ö.; Çağlar M. A.; Ertuğrul M.; Turgut G. Recent studies of theoretical gas sensing properties of 2D TMDC Janus materials. *Sens. Actuator A-Phys* **2025**, 383, 116236.

[40] El Beainou R.; Cote J.-M.; Potin V.; Martin N. Contrasted morphologies in nanostructured Janus W-Cu columns. *Mater. Today Commun.* **2021**, 27, 102331.

[41] Lintymer J.; Gavoille J.; N. Martin N.; Takadoum J. Glancing angle deposition to modify microstructure and properties of sputter deposited chromium thin films. *Surf. Coat. Technol.* **2003**, 174–175, 316-323.

[42] Hermann K. Crystallography and Surface Structure: An introduction for surface scientists and nanoscientists. **2011**, WILEY-VCH Verlag GmbH & Co. KGaA, Weinheim.

[43] Kim H.-J.; Lee J.-H. Highly sensitive and selective gas sensors using p-type oxide semiconductors: Overview, *Sens. Actuators B-Chem.* **2014**, 192 (2014) 607–627.

[44] Salthammer T. Very volatile organic compounds: An understudied class of indoor air pollutants. *Indoor Air* **2016**, 26, 25-38.

[45] Sekar A.; Varghese G. K.; Ravi Varma M. K. Analysis of benzene air quality standards, monitoring methods and concentrations in indoor and outdoor environment. *Heliyon*, **2019**, 5 (11):e02918.

[46] Khoshakhlagh A. H.; Mohammadzadeh M.; Ghobakhloo S.; Cheng H.; Gruszecka-Kosowska A.; Knight J. Health risk assessment from inhalation exposure to indoor formaldehyde: A systematic review and meta-analysis. *J Hazard Mater.* **2024**, 471, 134307.

[47] Richtwerte für 1-Propanol in der Innenraumluft. *Bundesgesundheitsbl.* **2022**, 65, 1226–1233.

[48] Kılıç A.; Tekin B.; Alev O.; Özdemir O.; Arslan L. C.; Büyükköse S.; Özturk Z. Z. Fabrication, characterization, and gas sensing performance of chromium doped WO₃ nanoflakes. *Semicond. Sci. Technol.* **2023**, 38, 035008.

[49] Zhanga Q.; Zhang H.; Xua M.; Shena Z.; Wei Q. A WO₃ nanorod-Cr₂O₃ nanoparticle composite for selective gas sensing of 2-butanone. *Chin. Chem. Lett.* **2018**, 29 (3), 538-542.

[50] Martin N.; Cote J.-M.; Boukhalfa H.; Potin V. Checkerboard-like structure in columnar W–Mo thin films. *Funct. Mater. Lett.* **2022**, 15, No. 06, 2251043.

[51] Mukherjee S.; Gall D. Structure zone model for extreme shadowing conditions. *Thin Solid Films* **2013**, 527, 158-163.

[52] Westwood W. D. Calculation of deposition rates in diode sputtering systems. *J. Vac. Sci. Technol.* **1978**, 15, 1.

[53] Boukhalfa H.; Potin V.; Martin N. Ballistic and thermalized regimes to tune structure and conducting proper-ties of W–Mo thin films. *Vacuum* **2022**, 204, 111347.

[54] Howard C. J.; Luca V.; Knight K. S. High-temperature phase transitions in tungsten trioxide-the last word? *J. Condens. Matter Phys.* **2002**, 14, No 3.

[55] Chang X.; Dong X.; Liu X.; Tong Y.; Li K.; Li Z.; Lu Y. Constructing a hexagonal/orthorhombic WO₃ phase junction for enhanced photochromism. *Opt. Mater.* **2023**, 142, 11413.

[56] Lee S.-H.; Cheong H. M.; Zhang J.-G.; Mascarenhas A.; Benson D. K.; Deb S. K. Electrochromic mechanism in a-WO₃₋ᵧ thin films. *Appl. Phys. Lett.* **1999**, 74, 242–244.

[57] Bai Y.; Qu S.; Jia Z.; Zhang L.; Zhu G.; Feng A.; Wu G.; Wu H. Cr₂O₃ nano-crystal anode materials with improved cyclic stability for lithium ion batteries. *J. Mater. Sci. Mater. Electron.* **2018**, 29, 11795–11800.

[58] Daniel M.F.; Desbat B.; Lassegues J.C.; Gerand B.; Figlarz M. Infrared and Raman study of WO₃ tungsten trioxides and WO₃, xH₂O tungsten trioxide hydrates. *J. Solid State Chem.* **1987**, 67 (2), 235-247.

[59] Garcia-Sanchez R. F.; Ahmido T.; Casimir D.; Baliga S.; Misra Prabhakar. Thermal effects associated with the Raman spectroscopy of WO₃ gas-sensor materials. *J. Phys. Chem.* A **2013**, 117 (50), 13825–13831.

[60] Fang Z.; Jiao S.; Wang B.; Yin W.; Liu S.; Gao R.; Liu Z.; Pang G.; Feng S. Synthesis of reduced cubic phase WO₃₋ₓ nanosheet by direct reduction of H₂WO₄·H₂O. *Mater. Today Energy* **2017**, 6, 146-153.

[61] Thanakkasaranee S.; Kasi G.; Kadhiravan S.; Arumugam A.; Al-Ghanim K. A.; Nadeem Riaz M.; Govindarajan M. Synthesis of tungsten oxide nanoflakes and their antibacterial and photocatalytic properties. *Fermentation* **2023**, 9, 54.

[62] Popescu A. G. M.; Tudose I. V.; Romanitan C.; Popescu M.; Manica M.; Schiopu P.; Vladescu M.; Suchea M. P.; Pachiu C. Raman study of novel nanostructured WO₃ thin films grown by spray deposition. *Nanomaterials* **2024**, 14, 1227.

[63] Baserga A.; Russo V.; Di Fonzo F.; Bailini A.; Cattaneo D.; Casari C.S.; Li Bassi A.; Bottani C.E. Nanostructured tungsten oxide with controlled properties: Synthesis and Raman characterization. *Thin Solid Films* **2007**, 515 (16), 6465-6469.

[64] Kelly A. G.; O'Suilleabhain D.; Gabbett C.; Coleman J. N. The electrical conductivity of solution-processed nanosheet networks. *Nat. Rev. Mater.* **2022**, 7, 217–234.

[65] Schipani F.; Aldao C. M.; Ponce M. A. Schottky barriers measurements through Arrhenius plots in gas sensors based on semiconductor films. *AIP Adv.* **2012**, 2, 032138.

[66] Choi S.; Bonyani M.; Sun G.-J.; Kyung Lee J.; Keun Hyun S.; Lee C. Cr₂O₃ nanoparticle-functionalized WO₃ nanorods for ethanol gas sensors. *Appl. Surf. Sci.* **2018**, 432, Part B, 241-249.

[67] Minu M.; Shinde P.V.; Samal R.; Rout C. S. A review on mechanisms and recent developments in p-n heterojunctions of 2D materials for gas sensing applications. *J. Mater. Sci.* **2021**, 56, 9575–9604.

[68] Upadhyay S.B.; Mishra R.K.; Sahay P.P. Cr-doped WO₃ nanosheets: Structural, optical and formaldehyde sensing properties. *Ceram Int.* **2016**, 42 (14), 15301-15310.

[69] Li Y.; Li F.; Li C.; Wei W.; Jiang D.; Zhu L.; Sun D.; Zhang X.; Ruan S. The preparation of Cr₂O₃@WO₃ hierarchical nanostructures and their application in the detection of volatile organic compounds (VOCs). *RSC Adv.* **2015**, 5, 61528–61534.

[70] Li F.; Ruan S.; Zhang N.; Yin Y.; Guo S.; Chen Y.; Zhang H.; Li C. Synthesis and characterization of Cr-doped WO₃ nanofibers for conductometric sensors with high xylene sensitivity. *Sens. Actuators B-Chem.* **2018**, 265, 355-364.